Journal of Natural Gas Science and Engineering 103 (2022) 104587

Contents lists available at ScienceDirect

Journal of Natural Gas Science and Engineering

journal homepage: www.elsevier.com/locate/jngse

# Chemical reactions of carbonate-rich mudstones with aqueous $CO_2$ and their impacts on rock's local microstructural and chemo-mechanical properties

Ravi Prakash [a], Pierre Christian Kana Nguene [b], Arash Noshadravan [a], Sara Abedi [a,b,*]

[a] Department of Civil Engineering, Texas A&M University, College Station, TX, 77843, United States
[b] Department of Petroleum Engineering, Texas A&M University, College Station, TX, 77843, United States

ARTICLE INFO

*Keywords:*
Carbonate-rich mudstones
Rock-CO2 interaction
Microstructural analysis
Micro-CT imaging
Coupled nanoindentation-EDS
Micro-scale chemo-mechanical characterization

ABSTRACT

Assessment of the structural integrity of carbonate-rich rocks subjected to acidic brine strongly relies on the understanding of the coupling between the chemical changes and the alteration of the mechanical properties of rocks. This study aims at an integrated microscale chemo-mechanical and microstructural characterization of carbonate mudstones exposed to $CO_2$-rich brine under high pressure and high temperature conditions. Digital image analysis was performed on X-ray micro-computed tomography (micro-CT) images to realize microstructural evolution and spatial distribution of pores and different material phases. This approach showed three distinct regions of porosity and carbonate content (resulting from dissolution and precipitation of calcium carbonates), which are critical for understanding the mechanical alteration of the rocks being investigated. Detailed analysis of the micro-CT images also revealed the preferred precipitation of calcium carbonates in pores parallel to the flow/reaction direction. Microscale chemo-mechanical testing performed using coupled grid nanoindentation and scanning electron microscopy-energy dispersive spectrometry (SEM-EDS) complemented the micro-CT results: dissolution zones close to the reacted surface were found to have lower hardness and indentation modulus while an increased values in adjacent precipitation zones was observed. Also, the thickness of the precipitation zones was found to be considerably higher in the direction of the bedding planes, which needs special attention in laminated rocks like shales and mudstones. The microstructural and mechanical properties of the microscale regions and the layered structure are expected to influence the overall mechanical properties and integrity of the rock. These results enhance our understanding of the microscale origin of the macroscopic mechanical alteration of carbonate-rich mudstones subjected to acidic brine.

## 1. Introduction

Understanding the effect of chemical reactions between carbonate rocks and acidic brine on the mechanical and microstructural properties of rocks is essential for many applications such as stability of geostructures, $CO_2$ storage, geothermal exploitation, and petroleum production to just name a few. In all these applications, the altered equilibrium between the injected fluid and the rock stimulates geochemical responses, mainly when $CO_2$ exists as a supercritical phase or in the form of aqueous $CO_2$ in the formation brine under high pressure and temperature conditions. For many applications, the structural integrity of the reacted formation is critical as it can lead to micro/macro cracks and high/low porosity zones, which can be potential pathways of $CO_2$ leakage or create zones of damage concentration (Gasda et al., 2004; Nordbotten et al., 2005). Previous geochemical studies have shown localized increasing and decreasing effects on rock permeability due to $CO_2$ attacks (Burnside et al., 2013; Busch et al., 2014; Hangx et al., 2015; Kampman et al., 2016; Minardi et al., 2021). A decrease in permeability is expected when carbonates precipitation seals the fractures and pores, while the dissolution of carbonate minerals, feldspar, iron oxides, and phyllosilicate minerals increases the permeability (Garcia et al., 2012; Gaus, 2010; Liu et al., 2012; Lu et al., 2012).

Aside from investigating the chemical responses, limited studies have explored the coupling of chemical changes to the alteration of mechanical properties of rocks after exposure to acidic brine, most of which have been applied to limestones and sandstones (Gunter et al.,

* Corresponding author. Department of Civil Engineering, Texas A&M University, College Station, TX, 77843, United States.
*E-mail address:* sara.abedi@tamu.edu (S. Abedi).

https://doi.org/10.1016/j.jngse.2022.104587
Received 5 November 2021; Received in revised form 12 April 2022; Accepted 20 April 2022
Available online 6 May 2022
1875-5100/© 2022 Elsevier B.V. All rights reserved.

1997; Liu et al., 2012; Rosenbauer et al., 2005). Such chemo-mechanical studies primarily focused the assessment of either the mechanical properties of bulk-reacted rock by means of compression tests and ultrasonic velocity measurements (Castellanza and Nova, 2004; Ciantia et al., 2015; Clark and Vanorio, 2016; Croizé et al., 2010; Fernandez--Merodo et al., 2007; Vanorio, 2015) or the micro-mechanical response of the reacted surface by means of small-scale measurements (Akono et al., 2019; Fuchs et al., 2019; Ilgen et al., 2018). These bulk rock tests and surface measurements do not account for the mechanical changes of different reaction zones formed in the reacted material. Understanding the mechanical properties of various material constituents in individual reaction zones is required to predict alterations in the bulk mechanical response and to assess the structural integrity of the rock following exposure to an acidic environment.

When exposed to acidic brine such as $CO_2$-rich brine, in general, dissolution and precipitation of carbonates, particularly calcite, are some of the dominant geochemical reactions detected in mudstones and shale rocks (Aman et al., 2018; Hangx et al., 2013, 2015; Ilgen and Cygan, 2016; Kharaka et al., 2006; Lamy-Chappuis et al., 2016). Calcite is prone to faster chemical reactions with $CO_2$ in comparison to hematite and silicate. Recent laboratory studies indicate that both the volume fraction and spatial distribution of calcite within the rock matrix influence the manner in which calcite dissolution and precipitation affect bulk mechanical properties (Arson and Vanorio, 2015; Hangx et al., 2015; Lamy-Chappuis et al., 2016). Therefore, the local alteration of the material caused by the geochemical reaction of calcite and the resulting mechanical response merit further investigation.

The present work is motivated by the aforementioned knowledge gaps. Specifically, the primary objective is to characterize the microstructural evolution and chemo-mechanical interactions of carbonate mudstones when exposed to $CO_2$-rich brine at high temperature and high pressure conditions. X-ray micro-computed tomography (micro-CT) imaging is performed to identify the different reaction zones and the spatial distribution of different minerals in these zones according to their densities and texture before and after the reaction. Nano-indentation coupled with scanning electron microscopy-energy dispersive spectrometry (SEM-EDS) is used to characterize the mechanical properties (indentation modulus and hardness) of different mineral constituents within individual reaction zones. The application of microstructural and chemo-mechanical characterization methods highlights key chemical reactions and the resulting mechanical properties changes across the depth of the reacted rock. The results of characterization techniques have the potential to provide instrumented data to inform and validate reactive transport models as well as chemo-mechanical models capable of simulating bulk mechanical response based on local properties.

## 2. Experimental techniques

### 2.1. Material

The present study uses outcrop samples from the Eagle Ford Formation. Table 1 details mineral composition, TOC, and porosity of samples obtained by X-ray diffraction analysis (XRD), rock eval pyrolysis, and pycnometer and dry bulk density measurements, respectively. Calcite is the main mineral component in the samples studied. The EF-1 sample, in particular, contains very small amounts of quartz, clay, and feldspar (Wang et al., 2017). The use of such a sample is justified by the fact that the relatively homogeneous nature of this particular sample enables us to study the effects of exposure to $CO_2$-rich brine on calcite with minimal influence from other minerals.

**Table 1**
Mass percent composition of Eagle Ford samples.

| Phase | Proportion (wt %) | |
|---|---|---|
| | EF-1 | EF-2 |
| Calcite | 94.4 | 65.1 |
| Dolomite | – | 7 |
| Quartz | 3.6 | 25.6 |
| Kaolinite | 1.1 | 1.5 |
| Orthoclase (Feldspar) | 0.9 | – |
| Hydrotalcite | – | 0.8 |
| TOC | 0.37 | 3.14 |
| Porosity | 5.2 | 8.99 |

Organic matter content was found to be 0.37% and 3.14% for EF-1 and EF-2 respectively. Interested readers are referred to (Donovan et al., 2012) for more information on the lithological and geochemical characteristics of EF-1 and EF-2 samples (which are referred to as Eagle Ford E and Eagle Ford B in (Donovan et al., 2012)).

### 2.2. Sample preparation

Prior to exposing the rock to $CO_2$, samples were cut from core plugs by the diamond saw into pieces 1 cm thick and 0.5–1 cm in diameter. The specimens were cut in directions parallel to bedding and normal to bedding. In order to study the microstructural evolution of samples due to chemical interactions, smaller samples (approximately 0.5 cm × 0.5 cm x 0.5 cm) were also prepared for micro-CT imaging. The surface of the micro-CT samples was polished prior to reacting with the fluid. The polishing consisted first of a coarse polishing with 400 grit hard perforated pads and then of an oil-based diamond suspension. Ultrasonic cleaning was subsequently performed to remove debris from the surface of the sample prior to dry polishing. In the next step, abrasive aluminum oxide discs of 12, 9, 3, 1, and 0.3 μm were used successively to achieve a smooth surface. A similar polishing procedure was followed prior to performing nanoindentation on the cross-section of reacted samples. As the intention was not to alter the microstructure, wettability, and pore structure of the studied rocks, the samples were simply ultrasonically cleaned in a n-decane solution that did not interact with the sample constituents and no further cleaning process was performed.

### 2.3. High pressure and high temperature reaction

After preparation, the mudstone samples were altered in a batch type Parr dissolution reactor made from titanium with a volume of 250 $cm^3$. Rock samples were submerged in 1 M (M) NaCl synthetic brine. The liquid to solid ratio was 19 by weight. The experimental temperature and pressure of 100 °C, 12.4 mPa (1800 psi) was used in this study. The relatively high temperature and liquid-solid ratio were selected to allow reasonable reaction rates for the batch type study. According to (Li et al., 2018), these experimental conditions lead to brine pH of 3.2. The $CO_2$ was injected into the reactor through a compressed gas cylinder. The pressure was controlled by a syringe pump attached to the reactor and the temperature was contained by a thermocouple, a heating jacket, and a temperature controller. The reaction continued for two weeks, long enough to allow rock samples to develop different reaction zones under the aforementioned conditions. We adopted slow depressurization to prevent rock spalling caused by fluid expansion. Batch reaction experiments were carried out for EF-1 and EF-2 samples separately to avoid any interaction between the reaction products of the two samples.

### 2.4. Pore-scale imaging of rock samples: image analysis and segmentation procedure

The Phoenix Nanotom micro-CT scanner and Thermo-Fisher Heliscan micro-CT scanner were used to obtain high resolution (voxel size ranging from 5 μm to 5.7 μm) images of mudstone samples before and after the reaction to study the microstructural evolution of samples as a result of chemical interaction.

Micro-CT imaging of the samples divides the representative volume into numerous grayscale image slices depending on the acquired resolution (Akhondzadeh et al., 2022). Each voxel in each image has a

grayscale value that corresponds to X-ray attenuation and is a function of density, atomic number and source energy (Hubbell and Seltzer, 1995). Fig. 1 shows a slice of micro-CT image of unreacted EF-1 sample and its intensity histogram. The lower gray level values (dark pixels in the image) represent the pores and background (air surrounding the sample) while the higher gray level values (lighter pixels in the image) represent calcite, quartz, clay and other dense inclusions.

Image segmentation is the process of providing threshold values to grayscale images to uniquely identify the different material phases (pores, clay minerals, quartz, calcite, and other dense minerals) and thus identify the spatial locations of these phases within the sample. In this study, noise removal and image segmentation take use of the Avizo software package (Scientific, 2015, 2018; Westenberger, 2008). Image segmentation is one of the most important steps in this analysis since all future microstructural characterization is dependent on its accuracy. Therefore, different segmentation methods at different stages and different samples according to the quality of the scans and composition of the rock samples were selected. The identification of pores and background of the EF-1 sample was carried out by Otsu's automatic thresholding, while texture supervised classification was implemented to identify other phases. For EF-2 sample, random forest machine learning classification and watershed segmentation method were used for the identification of pores and all other phases. Prior to implementing these segmentation techniques, image filtering was used for smoothening the images by removing the noise present in the form of speckles. Non-local means filtering algorithm (Buades et al., 2005) using an adaptive-manifolds (Gastal and Oliveira, 2012) based approach was applied. Non-local means filtering determines the new value of a voxel by comparing the neighborhood of all the voxels in a given search window. The weights are determined by the similarity between the neighborhoods. A small search window causes image because there is not enough structural information of the mineral grains is within that window and a large search window increases the processing time exponentially. Hence a search window of 10 voxels was selected (Scientific, 2018). The size of the local neighborhood of 3 voxels produced good filtering results for our samples. Following filtration, an automatic thresholding technique was implemented to identify the background and pores of the EF-1 sample. Otsu's segmentation method (Bostanabad et al., 2018; Hubler et al., 2017; Saxena et al., 2017) is the most commonly used technique for computing the automatic threshold on a grayscale image/volume. This method separates the image into two classes of pixels by maximizing the between-class variance. Once the pores and backgrounds were segmented, for the EF-1 sample, texture supervised classification was implemented to segment other phases i.e. calcite, quartz, clay, and pyrite. These different minerals can be easily recognized by their texture and intensity (Fig. 2(a)). These easily identifiable minerals, defined using markers, serve as training data. Using the similarity with the training data, each voxel was classified into different minerals using texture supervised classification. First order statistics (mean, variance, skewness, kurtosis, and variation) and histogram statistics were utilized to differentiate between light/dark, and irregular/homogeneous textures, while co-occurrence based features were utilized to differentiate between texture patterns. Fig. 2(b) shows the different phase volumes for one slice of an image of reacted EF-1, according to the above segmentation methodology. Since the X-ray attenuation coefficients of clay, quartz, and Al-rich zones (more explanation in Sec. 3.1) is very similar and the volumetric proportion of clay is very small (1%), the intensities associated with these phases are expected to be very similar in the micro-CT images. As such, all these phases have been combined for the segmentation.

For EF-2, the minerals in the scans were not very clearly identifiable due to the artifacts associated with image acquisition and reconstruction, hence more powerful tools such as random forest machine learning classification and watershed segmentation were used for the segmentation. Simple segmentation methods can produce inaccurate results, particularly in phase boundary regions. Unique threshold values cannot precisely differentiate between the phases since the edges are blurred due to the introduction of noise and partial volume effects during image acquisition. Also during segmentation of more than two phases, an undesirable intermediate coating phase of intermediate intensity (transition from high to low intensity) can be introduced between the phases. To address these issues in phase identification, watershed segmentation was employed. Before using watershed segmentation, random forest machine learning was used to generate accurate labels for individual phases. Training data is provided by assigning phase labels (i.e. pores, calcite, dolomite, quartz, Al-rich zones and pyrite) on grayscale input volume. It is important that variability in mineral intensity is well represented in training labels. As a result, several labels of the same minerals were provided on several images. Using these training labels, random forest multi-class identification was performed on a part of the sample to preview the classification results. Once appropriate labels were identified, the classification process could be launched to the full

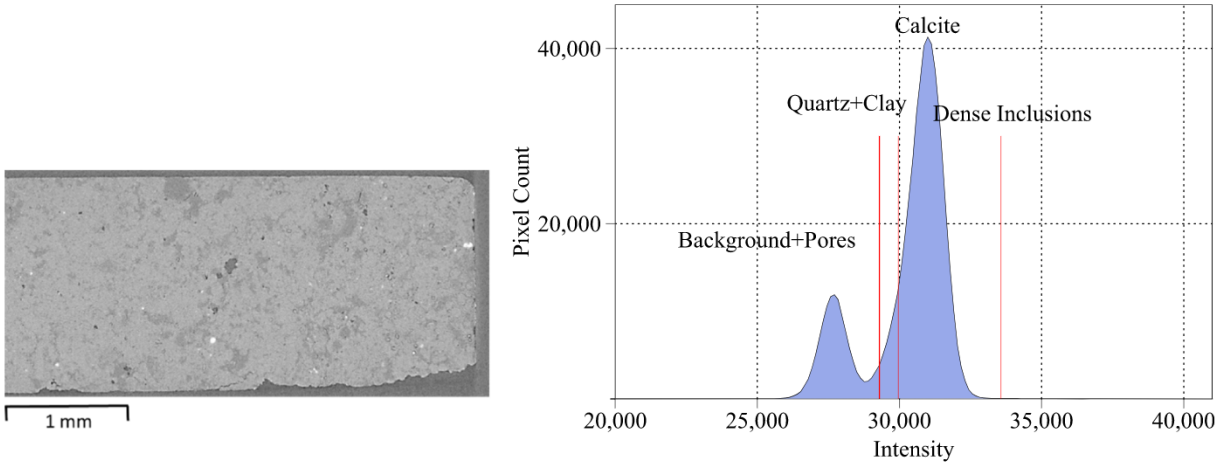


**Fig. 1.** (a) A slice of micro-CT image of unreacted EF-1 sample (b) Intensity histogram of the image.

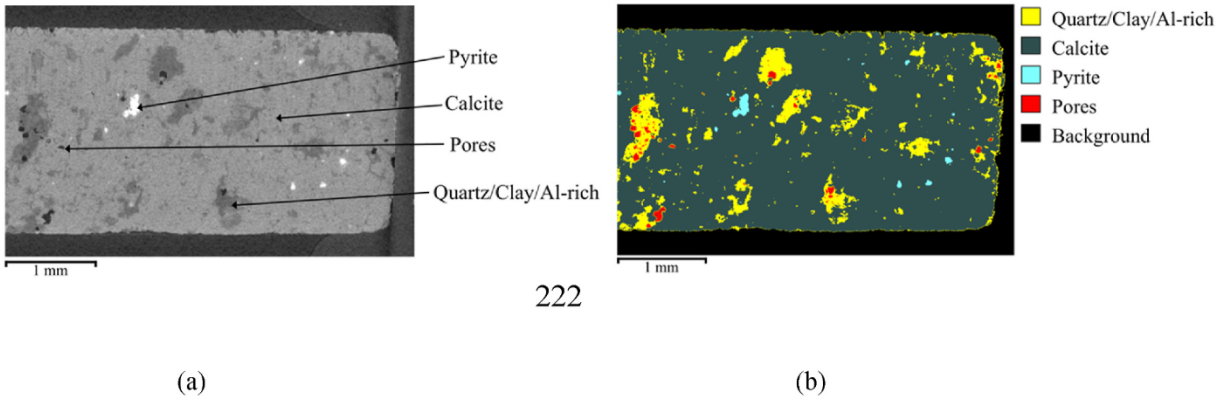


**Fig. 2.** One slice of reacted EF-1 sample, (a) post filtering (b) post segmentation, showing different mineral constituents.

volume. If this generated classification did not generate any false labels, watershed segmentation was performed to identify all the phases. Fig. 3 shows an image slice of reacted EF-2 shale with different constituent phases, segmented according to the aforementioned method.

Because mudstones have the majority of their pores at the nano-scale level and the voxel dimensions are 5 μm and 5.7 μm for EF-1 and EF-2 scans, respectively, not all the pores can be captured in our images. Therefore, unidentified pores were assumed to be evenly distributed throughout the phases. Table 2 compares the volume percentage of different material phases segmented by the aforementioned procedure in the unreacted portion of the samples (the middle portion) and the volume percentage acheived by analyzing XRD results. In calculating the volume percentages from the XRD results, we considered a uniform distribution of organic matter across all material phases. Densities of the main mineral constituents are accounted for according to Mashhadian et al. (2018b).

**Table 2**
Volume percent composition of Eagle Ford samples obtained from segmentation of micro-CT images and the comparison with the volume percent composition obtained from XRD analysis. It should be mentioned that the porosity identified by segmentation of micro-CT images is micro-porosity (with dimensions bigger than voxels' size).

| Phase | EF-1 | | EF-2 | |
|---|---|---|---|---|
| | XRD (vol %) | Micro-CT (vol %) | XRD (vol %) | Micro-CT (vol %) |
| Calcite | 89.4 | 93.2 | 59.0 | 53.8 |
| Dolomite | – | – | 6.0 | 14.9 |
| Quartz/ Clay | 4.6 | 4.3 | 25.1 | 25.2 |

### 2.5. Chemo-mechanical analysis of rock samples

#### 2.5.1. Nanoindentation test

To measure the mechanical properties of different microstructural regions within the reacted rock samples, indentation modulus and hardness were obtained by grid nanoindentation testing performed on polished cross-sections (Hysitron TI 950). Cross-section samples were prepared by cutting and polishing reacted rock samples perpendicular to the exposed surface. In the indentation test, a diamond Berkovich tip was used to probe the samples at a loading rate of 0.48 mN/s to a maximum load of 4.8 mN, holding it for 10 s, and then unloading from the surface at the same rate (Abedi et al., 2016a; Martogi and Abedi, 2019, 2020; Mashhadian et al., 2018b). The indentation modulus ($M$) and Hardness ($H$) were then calculated by

$$M = \frac{\sqrt{\pi}}{2}\frac{S}{\sqrt{A_c}} \tag{1}$$

$$H = \frac{P_{max}}{A_c} \tag{2}$$

where, $S = \frac{dP}{dh}$ represents the experimentally measured contact stiffness (initial unloading stiffness) measured at the maximum load $P_{max}$, and $A_c$ is the projected area of the elastic contact (Abedi et al., 2016b; Mashhadian et al., 2018a; Memon et al., 2021). The latter is a function of the contact depth, $h_c$ and the indenter shape. Due to the heterogeneous nature of different microstructural regions of the reacted sample, we implemented grid indentation technique which consists of performing a large (620 and 400 indents for EF-1 and EF-2 sample, respectively) set of indentation tests on the material surface.

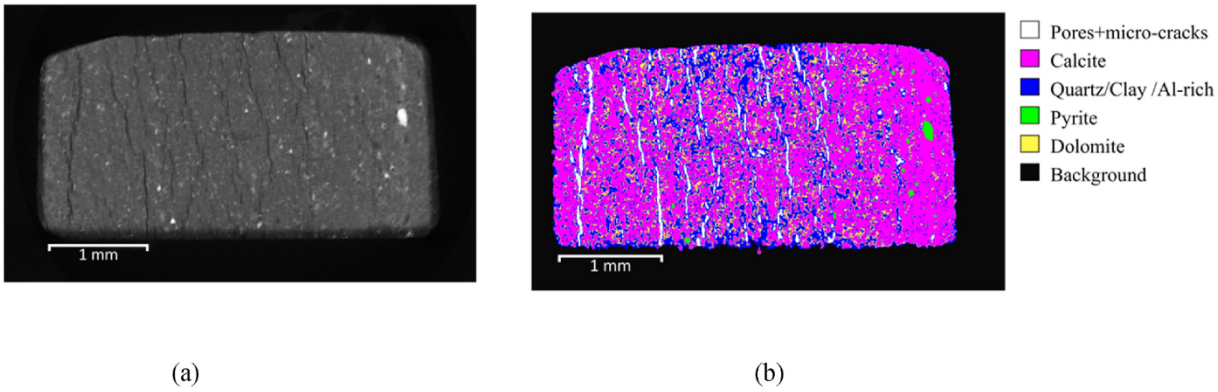


**Fig. 3.** One slice of reacted EF-2 sample, (a) post filtering (b) post segmentation, showing different mineral constituents.

*2.5.2. SEM-EDS and multispectral clustering analysis*

The compositional analysis in this study made use of the SEM-EDS method. This analysis was intended to produce a cluster map by identifying the main mineral constituents of the sample. Thereafter, these cluster maps were used to identify the overall change and, more importantly, the variation in mechanical properties, i.e. indentation modulus and hardness of different phases along with the reaction depth. To achieve this, the elemental composition of each indentation point needed to be distinctly identified. For this purpose, EDS maps were acquired over the same area of the indentation grid (Abedi et al., 2016a; Sharma et al., 2019; Slim et al., 2018). A sequence of image analysis (refinment, noise removal, and thresholding) was performed on the EDS elemental maps using the freeware software ImageJ (Schindelin et al., 2012). These EDS images were then superimposed using different color channels to form a multispectral image. The aforementioned series of analyses were performed on the main constituent elements namely Si, Ca and Al. These elemental maps were mathematically merged using RGB color channels. At once, only three elemental maps were used to produce a multispectral image. Following Lydon's unsupervised clustering procedure (Chancey et al., 2010; Lydon, 2005), using the clustering analyzer in the Multispec program, a cluster map was produced having multiple phases (Prakash et al., 2021). Fig. 4 shows the cluster map for the EF-1 sample showing distinct phases based on multispectral analysis. Locating the indentation points on the EDS map is very crucial for identifying the minerals at those points and is therefore done with great precision. Several images of the sample were taken under an optical microscope before and after performing the indentation. These optical images were then compared with backscattered SEM images to accurately locate the indentation points. Once the pixel locations of the indentation points are determined on the cluster map, the material phase at each indentation point was known. The above analysis required high resolution EDS images. To achieve that, EDS was configured to acquire elemental maps with a resolution of 1024x768 pixels covering the width of 800–900 μm and a minimum of 15 frames was collected for

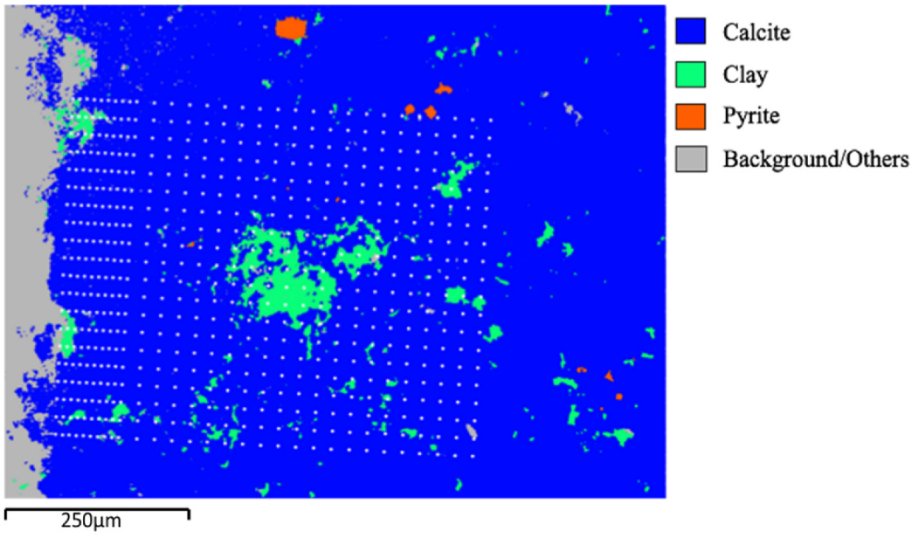


(a)

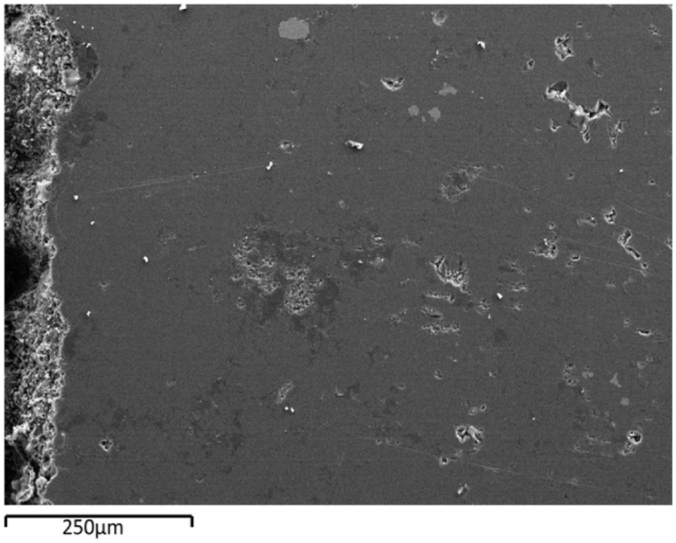


(b)

**Fig. 4.** (a) Indentation grid pattern on multispectral image of reacted EF-1 sample showing different material phases. (b) SEM image of the same location.

each sample. Also, the samples were coated with a 25 nm thin conductive layer of Platinum–Palladium to minimize charging.

## 3. Results and discussion

### 3.1. Microstructural evolution of reacted samples: results from micro-CT image analysis

#### 3.1.1. Pore statistics

Following the procedure outlined in 2.4, micro-CT images of both EF-1 and EF-2 samples were segmented to identify different material phases of the sample volume (Figs. 2 and 3). The smaller peak in the intensity histogram (Fig. 1) corresponds to the pores and background and the larger peak represents the rest of the minerals present in the sample. In order to calculate the volume of pores due to dissolution on the surface of the reacted sample, a convex hull i.e. smallest convex polygon encapsulating the binary image was created. The volume encapsulated by this convex polygon on the reacted surface was considered to be the surface dissolution volume. This assumption should be accurate as the rock sample used was well polished before the reaction. To obtain the pores in a volume, all the abovementioned analyses were automated on individual images.

Fig. 5 shows the variation of porosity with respect to distance from the reacted surface for both parallel to bedding and normal to bedding directions for both the samples. These values were obtained by averaging the porosities from the stack of 1300 and 700 images for EF-1 and EF-2 samples, respectively. It should be noted that the porosity identified by segmentation of micro-CT images represents the micro-porosity with dimensions larger than the voxel size, however we refer to them as porosity for brevity.

For EF-1, parallel to the bedding plane, the trend shows dissolution at the surface (increase in porosity) up to a depth of 80 μm. It also suggests precipitation (reduction in porosity) follwoing dissolution depth i.e. from 80 to 600 μm. After the precipitation depth, constant porosity is observed that indicates that there is no reaction in the sample. The dissolution depth is found to be identical in the direction perpendicular to the bedding plane, whereas the reach of the precipitation zone is limited to 300 μm. Therefore, the total reaction depth is 600 μm and 300 μm in parallel to bedding and normal to bedding directions, respectively. This data implies that the depth of reaction is a function of the orientation of the bedding plane and at the time scale of our experiments, the depth of penetration is almost doubled when the reaction front is parallel to the bedding plane as compared to perpendicular flow. For sample EF-2, Fig. 5 (b) shows that in the direction parallel to the bedding plane, the porosity is constant after a 120 μm dissolution region. This constant porosity can be the result of the formation of depth-long micro-cracks (Fig. 3) that contaminate the results of micro-CT. These micro-cracks were not present in the micro-CT volume of the same sample before the reaction. However, perpendicular to the bedding plane, there is a decrease in the dissolution depth (up to 60 μm) while a precipitation zone from 60 to 450 μm can be seen. Also from the micro-CT images, it is evident that micro-cracks are absent in the precipitation region in perpendicular to bedding direction. This filling of micro-cracks can be attributed to the precipitation of calcium carbonates in this region. These micro-cracks were absent in EF-1 sample and were present in EF-2 sample with a higher concentration of both micro-porosity (Fig. 5 and Table 1) and total porosity and higher quartz concentration (25.6%). Micro-cracks might form near regions with large pores due to intense redistribution of stress within the adjacent rock frame (Clark and Vanorio, 2016; Grgic, 2011) or they might emerge at the boundaries between different phases due to the presence of defects or elastic mismatch. It is also apparent from the segmented image (Fig. 3) that micro-cracks are formed in the vicinity of areas with high quartz concentration in the EF-2 sample. It should be noted that the boundary between the micro-cracks and the solid phase is blurred and cannot be identified with great precision. Although watershed segmentation was has been performed to resolve this issue, some regions surrounding the micro-cracks were identified as quartz due to the imprecision of the segmentation procedure. The formation of micro-cracks cannot be attributed to the swelling nature of clay particles due to the very small amount and comparatively similar amount of clay particles in both samples.

Rock samples used in this study were cuboidal in shape with their top surfaces cut perpendicular to bedding direction (called X1 surface in this study) with two sides of the samples in the direction parallel to the bedding (X3 surface). For both reacted EF-1 and EF-2 samples the orientation and aspect ratio of the pores were calculated by fitting an ellipse that has the same second-moments as the pore region. The calculation of pore orientation is shown in Fig. 6. The horizontal dashed line indicates direction parallel to the bedding plane. Therefore, $\theta = 90^{\circ}$ represents pores aligned perpendicular to the bedding planes and $\theta = 0^{\circ}$ represents pores arranged parallel to the bedding plane. As much as 39.5% of pores in EF-1 sample and 33.6% in EF-2 sample were found to have an aspect ratio of one (i.e. circular pores) which implies no preferred orientation for these pores. Therefore, to achieve the preferred orientation of the remaining pores, all pores with an aspect ratio of 1 were eliminated.

Fig. 7 shows the histogram of the pore orientation for the reacted EF-1 sample in the dissolution, precipitation, and no reaction zones for both X1 (a) and X3 (b) surfaces. As mentioned earlier, zero degrees of orientation corresponds to pores aligned parallel to the bedding plane, while 90° corresponds to the pores aligned perpendicular to the bedding plane. For no reaction zone in the EF-1 sample and the X1 surface, no preferred porosity orientation is observed (an almost equal number of pores are detected in both parallel and perpendicular to the bedding plane). While in the dissolution and precipitation zones, more pores are seen to be in the direction perpendicular to the bedding plane, which is perpendicular to the direction of the reaction/flow. This suggests the

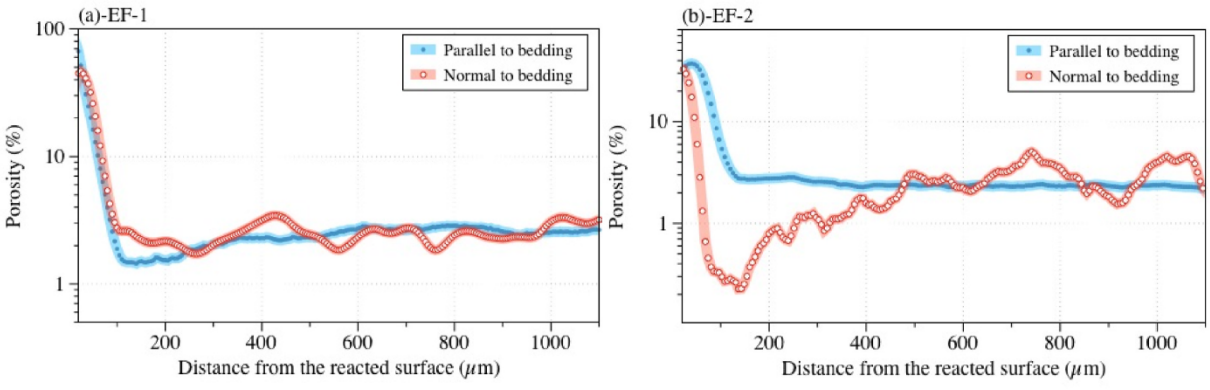


**Fig. 5.** Variation of porosity versus distance from the exposed surface, parallel and normal to bedding plane. (a) EF-1 (b) EF-2.

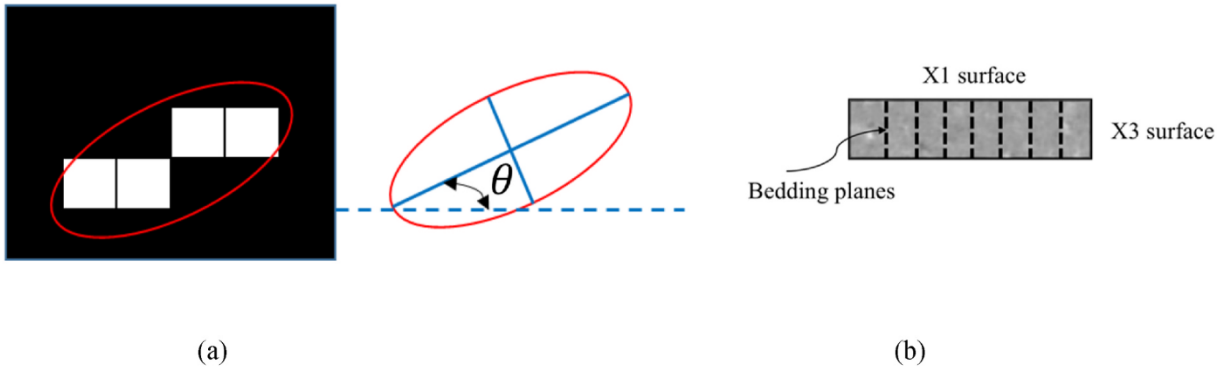


**Fig. 6.** (a) Illustrating the calculation of orientation of pores. Orientation is the angle between the horizontal dotted line which represents bedding orientation and major axis of the ellipse. (b) cuboidal shaped samples with X1 surface (cut perpendicular to bedding direction) on top and X3 surfaces (cut parallel to the bedding direction) on sides.

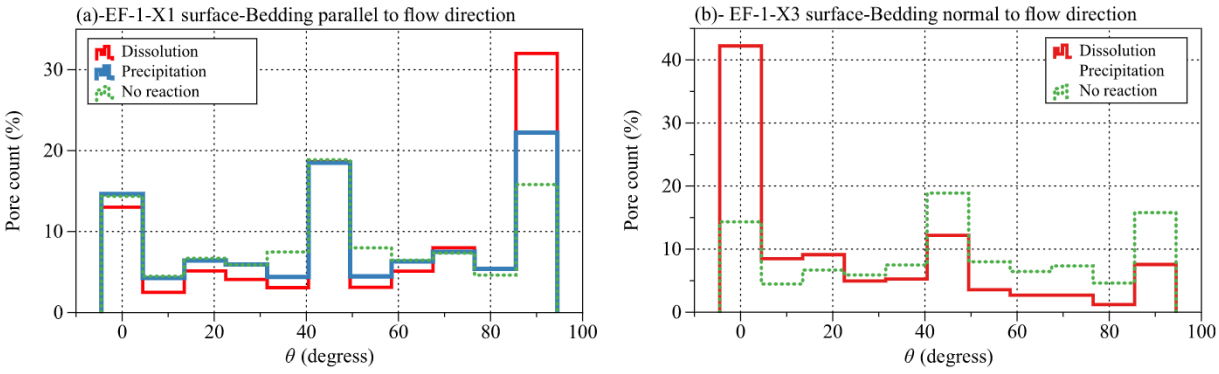


**Fig. 7.** Histograms showing the orientation of pores for reacted EF-1 sample in dissolution, precipitation and no reaction zone. (a) X1 surface, bedding parallel to flow direction (b) X3 surface, bedding normal to flow direction. Zero degrees orientation corresponds to pores aligned parallel to the bedding plane while 90° corresponds to the pores aligned perpendicular to the bedding plane.

preferred precipitation of calcium carbonates into pores parallel to the bedding plane or the direction of the reaction. The dissolution process creates pores in both the direction of reaction and perpendicular to it; however, the pores in the direction of the reaction filled up faster during the precipitation process. The same is also the case for the X3 surface; while there is no preferred orientation of pores in the no reaction zone, more pores are observed in the direction parallel to the bedding plane, which is perpendicular to the direction of the reaction in the dissolution and precipitation zones. This observation supports our argument concerning the preferred precipitation of calcium carbonates in pores aligned with the direction of the reaction.

The preferred orientation of pores is even more evident in the reacted EF-2 sample. As can be seen in the segmented micro-CT image of EF-2 shown in Fig. 3, parallel to the bedding plane, numerous vertical micro-cracks are formed that run throughout the thickness of the sample while there are no cracks normal to the bedding plane. This difference in the orientation of pores and micro-cracks may lead to the difference in permeability in parallel and perpendicular to the bedding directions (transverse isotropic permeability). Fig. 8 shows the histogram of the orientation of pores for the reacted EF-2 sample in different reaction zones for both X1 (a) and X3 (b) surfaces. For the reaction from the X1 surface, we divided the volume of the sample into two regions of

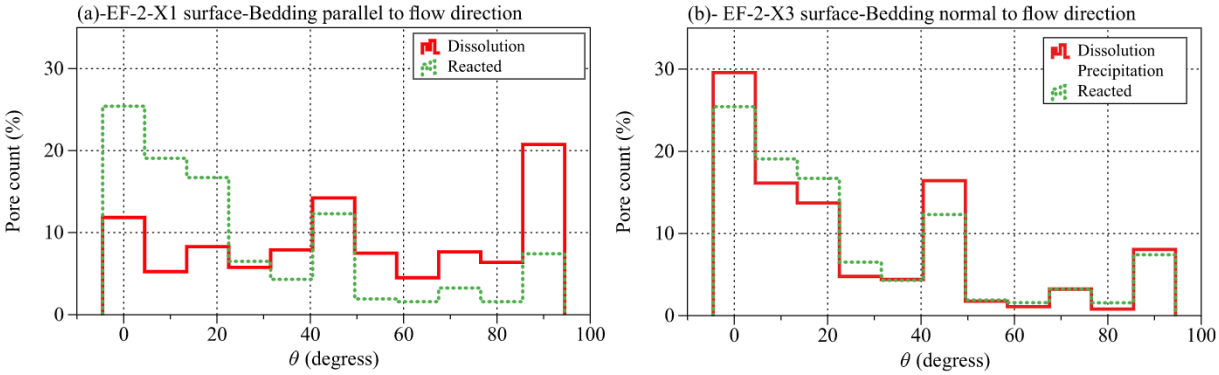


**Fig. 8.** Histograms showing the orientation of pores for reacted EF-2 sample in dissolution, precipitation and reacted zone. (a) X1 surface, bedding parallel to flow direction (b) X3 surface, bedding normal to flow direction. Zero degrees orientation corresponds to pores aligned parallel to the bedding plane while 90° corresponds to the pores aligned perpendicular to the bedding plane.

dissolution and reacted zones (without precipitation and no reaction zones). This is due to contamination of the reaction depth due to the formation of micro-cracks for this side of the sample. It should be noted that the porosity associated with micro-cracks is separated and is not considered in this calculation by the way of considering the size or area of the cracks. Any pore with a surface in excess of 50 voxels is considered as a micro-crack. The threshold of 50 voxels for pores to be considered as micro-cracks is achieved through multiple trials and errors and manual image verification.

For the X1 surface, similar to the EF-1 sample, in the dissolution zone, more pores are observed in the direction perpendicular to the direction of flow/reaction compared to the reacted zone. In the reacted zone, most of the pores are aligned in the direction of the bedding plane. Given that the sample has reacted throughout the depth, these pores could be the pores that allow the flow of fluid in the parallel to bedding direction. It should be emphasized again that these pores do not include micro-cracks. For the X3 surface, still similar to the X3 surface of the EF-1 sample, more pores are observed in the direction perpendicular to the reaction in the dissolution and precipitation zones. These observations corroborate the previous remark concerning the preferred precipitation of calcium carbonates in pores aligned with the flow direction.

### 3.1.2. Phases of reacted samples

To recognize the dissolving and precipitating phases in different zones, the variation of different material phases in EF-1 and EF-2 samples is also studied. Fig. 9 (a) and (b) show the volume fraction of different material phases as a function of distance from the reacted surface for the EF-1 sample in the direction parallel to the bedding plane and for the EF-2 sample in the direction normal to the bedding plane, respectively. It is evident that the dissolution of calcite is the dominant reaction at the surface according to the following equations.

$$CO_2(g) \leftrightarrow CO_2(aq) \tag{3}$$

$$CO_2(aq) + H_2O \leftrightarrow H_2CO_3 \tag{4}$$

$$H_2CO_3 + CaCO_3 \leftrightarrow Ca^{2+} + 2HCO_3^- \tag{5}$$

Reaction 3 is the dissolution of $CO_2$ in water and is dependent on temperature and pressure conditions, which further initiates the formation of carbonic acid (reaction 4). Calcite dissolves into the resultant solution according to reaction 5. The high aqueous concentration of dissolved calcium and carbonate ions leads to an increase in the rate of precipitation. Calcium carbonate is deposited within the precipitation zone according to the following reactions (Bachu et al., 1994; Gunter et al., 1997; Le Gallo et al., 2002; Rosenbauer et al., 2005).

$$H_2CO_3 \leftrightarrow H^+ + HCO_3^- \tag{6}$$

$$HCO_3^- \leftrightarrow H^+ + CO_3^{2-} \tag{7}$$

$$Ca^{2+} + CO_3^{2-} \leftrightarrow CaCO_3\downarrow \tag{8}$$

Reactions 6 and 7 represent the formation of carbonate ions through the liberation of protons from the carbonic acid. These carbonate ions then react with the dissolved $Ca^{2+}$ (formed through dissolution) in the brine to form the precipitate of calcium carbonate.

An important observation is the formation of Al-rich zones and Al-precipitates (e.g., gibbsite) in the two samples. These Al-rich zones are formed as a result of weathering of Al-bearing minerals in the rocks at a slightly acidic pH (Lee et al., 2019; Prakash et al., 2021; Shvartsev, 2012). Al-bearing minerals such as phyllosilicate clays are often the source of Al for the formation of aluminum hydroxide phases. The formation of these Al-rich zones are found in both EF-1 and EF-2 samples (Fig. 9). As explained in Sec. 2.4, since the X-ray attenuation coefficients of the Al-rich zones, clay, and quartz are very similar, these phases are combined for the segmentation of the two samples.

For both samples, there is an increased concentration of quartz/clay/Al-rich zones in the dissolution zone. This increase is caused by the deposition of clay minerals and the formation of Al-rich zones close to the exposed surface. The decrease in the concentration of quartz/clay/Al-rich zones in the precipitation zone is the result of the clay dissolution and micro-crack formation in quartz grains and the precipitation of carbonates in those micro-cracks which remove the quartz particles (see Fig. 10).

### 3.2. Changes in microscale mechanical properties

By employing nanoindentation coupled with EDS (Prakash et al., 2021), the hardness and indentation modulus of individual material phases located in different reaction regions on the polished cross-section of samples can be obtained and compared with similar phases in the unreacted region.

Changes in the mechanical properties of rocks following a $CO_2$ attack under a variety of environmental conditions have been reported earlier (Akono et al., 2019; Ciantia and Hueckel, 2013; Fernandez-Merodo et al., 2007; Fuchs et al., 2019; Ilgen et al., 2018; Vanorio, 2015). However, much less attention has been paid to the formation of different reaction zones in the reacted sample and their associated mechanical alterations due to dissolution and precipitation of new material phases. This new information is an important link to the altered mechanical properties of bulk samples. To study these variations, grid indentations with 600–800 indentation points were performed on the polished cross-sections of Eagle Ford samples exposed to $CO_2$-rich brine. These indent points start as close as 15 μm from the reacted surface (dissolution zone) traversing the precipitation zone, and reaching the unreacted zone of the sample. Adjacent to the exposed surface, a relatively smaller spacing of 10 μm was preferred on EF-1 sample in order to adequately capture the variation in mechanical properties in the dissolution zone. The indentation spacing was then increased to 25 μm to examine the

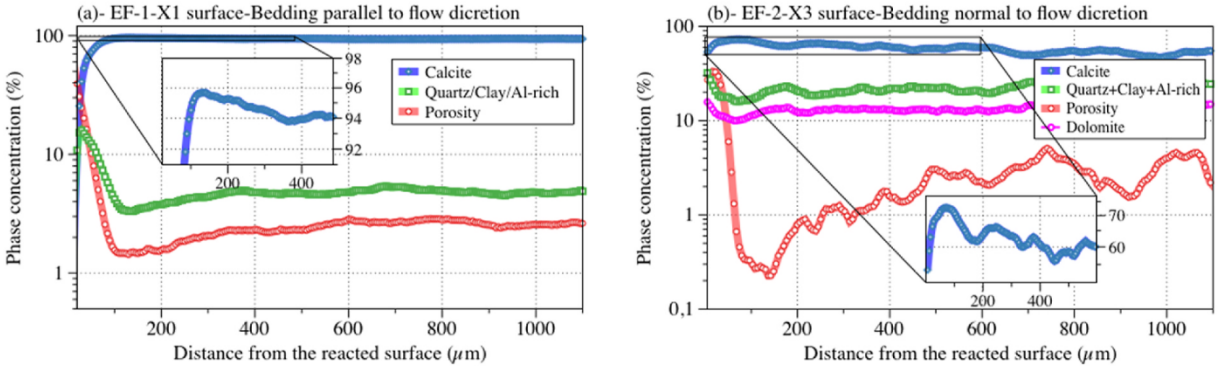


**Fig. 9.** Volume fraction of different material phases as a function of distance from the reacted surface for (a) EF-1 sample in the direction parallel to the bedding plane (b) EF-2 sample in the direction normal to the bedding plane.

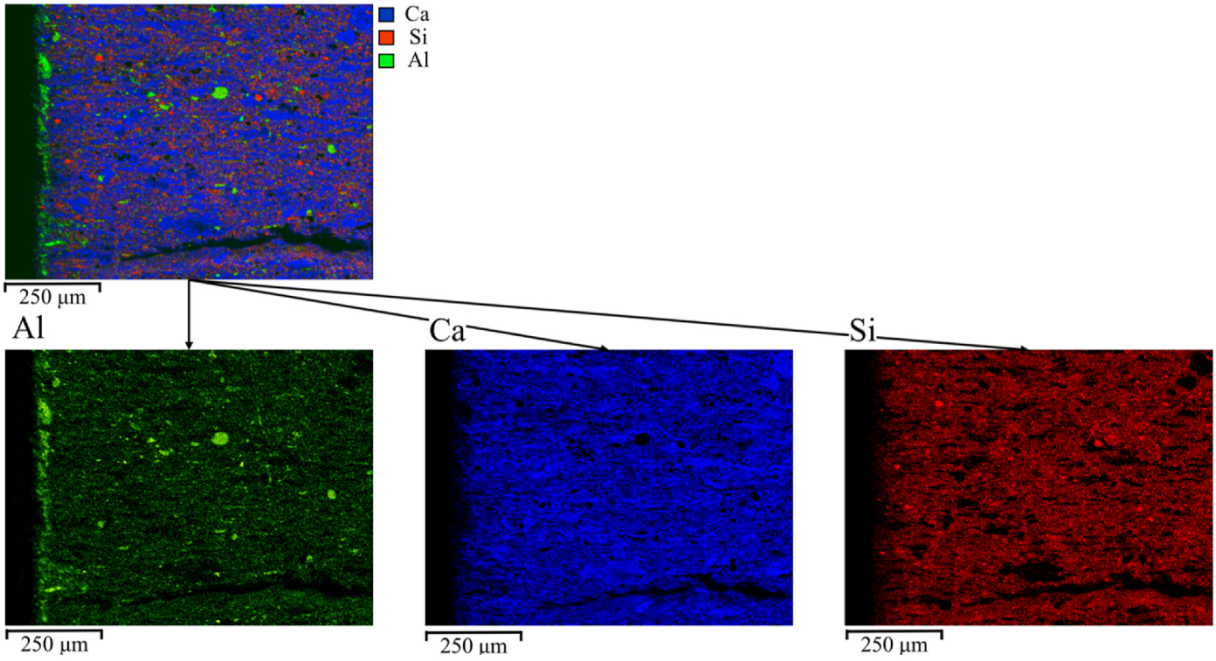


**Fig. 10.** Raw EDS combined map (Ca + Si + Al in the top map) and single elemental map (bottom maps) of reacted EF-2 sample showing the formation of Al-rich zones.

extent or depth of the reaction. For the EF-2 sample, the 25 μm spacing was used on the cross-sectional area of the sample. Fig. 4(a) displays the location of one of the indentation grids over the multispectral image in the EF-1 sample. Indentation measurement coupled with EDS were performed close to the reacted surface and in the direction parallel and perpendicular to the bedding plane for EF-1 and EF-2 samples respectively.

Making use of the multispectral image, the indentation points over the calcium carbonate phase are identified. Fig. 11(a) shows the average (over each indentation column) mechanical properties of the calcium carbonate phase in sample EF-1 along the depth of reaction for one of the grids. A similar trend in mechanical properties was observed in all other indentation grids performed. The observed trend clearly shows the presence of dissolution, precipitation, and no reaction zones, despite some scatter in the indentation results within each zone due to the local porosity variations within the calcium carbonate phase in different reaction regions.

As expected, modulus and hardness are found to be lower close to the exposed surface. These low values are consistent with the observed high porosity zone from micro-CT analysis. This indicates the formation of a dissolution zone where the specimen is weakened due to the partial dissolution of the calcium carbonate phase. After this region, we find a harder region which is established by the increase in hardness and modulus values. This increase in mechanical properties can be explained by the precipitation of calcium carbonate in this zone. Micro-CT results confirm this precipitation of calcium carbonate by displaying a decrease in porosity and an increase in the percentage of calcium carbonate in this region (Fig. 9). Beyond the precipitation zone, the modulus and hardness curves decrease and converge to a constant value, which indicates the end of the reaction front or the onset of no reaction zone.

A similar trend is observed for the EF-2 sample. Fig. 11 (b) shows the plot of the indentation modulus across the depth of the reaction for the calcium carbonate phase. Each point in the Figure represents the average of indentation results of points belonging to the calcium carbonate phase within each column of the indentation grid. Three different regions of mechanical properties can be differentiated: First, a region of low mechanical properties (~30 GPa of indentation modulus) confined to approximately 120 μm. This region represents the dissolution zone where calcium carbonate partially dissolves, leaving the region more porous with subsequent lower mechanical properties. The dissolution region is followed by the precipitation zone exhibiting enhanced mechanical properties compared to the remainder of the sample to a depth of about 350 μm. For both EF-1 and EF-2 samples, the results from micro-CT complement nanoindentation results and reveal

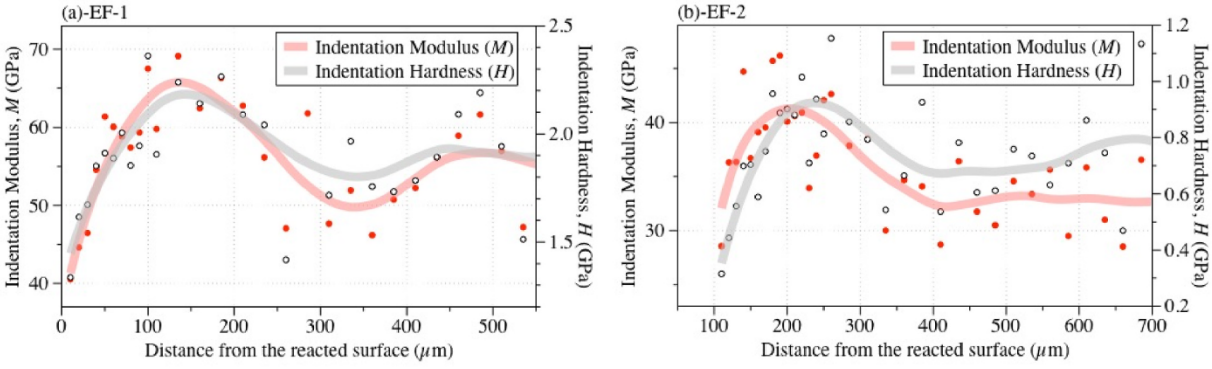


**Fig. 11.** Variation of Indentation modulus across reaction depth of the carbonate phase for (a) EF-1 sample and (b) EF-2 sample.

that a change in the porosity of the reactive constituents is the dominating factor for the observed changes in microscale mechanical properties.

## 4. Conclusions

Linking small-scale mechanical and microstructural properties to macroscale mechanical performance.

The multidisciplinary approach presented in this study managed, for the first time, to obtain the alteration of microstructural and mechanical properties of individual material phases in individual reaction zones developing in $CO_2$-exposed mudstone samples. Specifically, the results stressed the importance of investigating the role of different reaction zones (dissolution and precipitation regions) on macroscale mechanical properties. Earlier studies have shown the deteriorating role of $CO_2$ attack on rock samples. For example, Vialle and Vanorio (2011) reported a noticeable reduction in elastic properties of carbonate rocks upon interaction with $CO_2$-rich brine. However, local variations in microstructural features and mechanical properties of individual material constituents in different reaction regions and their implication on the overall mechanical properties of the rock has not been studied before. This study revealed the changes in the rock microstructure that led to variations in the mechanical properties of carbonate mudstones. In the specific case of this study, our results show that alteration of the porosity of the reactive material phases is the dominating factor for the change in the multiscale mechanical properties.

Our results showed three distinct regions of porosity and carbonate content that are critical for understanding the mechanical alteration of the rocks under study. Micro-scale chemo-mechanical tests carried out by coupled grid nanoindentation and SEM-EDS complements the results of micro-CT: dissolution zones near to the reacted surface were found to have lower hardness and indentation modulus while we observed an increased value in the adjacent precipitation zones. The thickness of the dissolution zone is found to be the same in direction parallel and perpendicular to the bedding plane (in EF-1 sample) while the extent of the precipitation zone indicates directional bias. Detailed analysis of micro-CT images also revealed the preferred precipitation of calcium carbonates in pores parallel to the direction of flow/reaction. At the large scale, the mechanical properties of bulk materials are affected by changes in hardness and modulus at smaller scales. The arrangement of how strong and weak small-scale components are compiled might lead to the weakening or strengthening of the bulk material. Further studies is required to link the effect of microscale mechanical alteration on the resulting macroscopic mechanical properties.

Although for samples with very high (~90%) carbonate content, micro-cracks have not been observed following chemical reactions in our study, the mechanical weakness of the dissolution region can facilitate the formation of fractures, channels, and gaps between the dissolution and precipitation regions. This phenomenon has been observed in other geomaterials subjected to reactive brine (Li et al., 2015). It is therefore very important to track the development of the dissolution region as it could reduce the integrity of the rock. Rocks like EF-2, with a relatively higher amount of micro-porosity and higher volume of quartz and lesser carbonates, might be subjected to a higher risk of instability as several cracks are observed throughout the sample.

As demonstrated by the results of this study, an important way to understand rock alteration is within a combination of chemical, microstructural, and mechanical analysis performed at multiple scales. We obtained the mechanical properties of the minerals in each region of attacked samples. This type of analysis can be used to calibrate reactive transport models as well as chemo-mechanical models capable of simulating bulk mechanical response based on local properties. Through model calibration, we can enhance our understanding of the mechanisms involved in rock/reactive fluid interaction and the role of microscale mechanical properties on bulk material response. This enhanced understanding of the mechanisms involved will translate into a more robust prediction based on different thermodynamics involved for systems under different environmental and geological conditions. The experimental methodology developed in this work presents a stepping stone for future investigations on the coupling of chemical and mechanical effects.

## Credit author statement

Ravi Prakash: Formal analysis, Investigation, Validation, Writing. Pierre Christian Kana Nguene: Formal analysis, Investigation, Validation. Arash Noshadravan: Conceptualization, Supervision, Writing – review & editing. Sara Abedi: Conceptualization, Writing – review & editing, Supervision, Project administration, Funding acquisition.

## Declaration of competing interest

The authors declare that they have no known competing financial interests or personal relationships that could have appeared to influence the work reported in this paper.

## Acknowledgment

The authors acknowledge the use of the Materials Characterization Facility at Texas A&M University and thank Dr. Yordanos Bisrat and Dr. Wilson Serem for their technical assistance. Acknowledgment is made to the donors of the American Chemical Society Petroleum Research Fund (PRF 60545- ND9) and to the National Science Foundation (Grant CMMI-2045242) for support of this research.

## References

Abedi, S., Slim, M., Hofmann, R., Bryndzia, T., Ulm, F.-J., 2016a. Nanochemo-mechanical signature of organic-rich shales: a coupled indentation–EDX analysis. Acta Geotechnica 11, 559–572.

Abedi, S., Slim, M., Ulm, F.-J., 2016b. Nanomechanics of organic-rich shales: the role of thermal maturity and organic matter content on texture. Acta Geotechnica 11, 775–787.

Akhondzadeh, H., Keshavarz, A., Awan, F.U.R., Zamani, A., Iglauer, S., Lebedev, M., 2022. Coal cleat network evolution through liquid nitrogen freeze-thaw cycling. Fuel 314, 123069.

Akono, A.-T., Kabir, P., Shi, Z., Fuchs, S., Tsotsis, T.T., Jessen, K., Werth, C.J., 2019. Modeling $$\hbox {CO} _2 $$-induced alterations in Mt. Simon sandstone via nanomechanics. Rock Mech. Rock Eng. 52, 1353–1375.

Aman, M., Espinoza, D.N., Ilgen, A.G., Major, J.R., Eichhubl, P., Dewers, T.A., 2018. CO2-induced chemo-mechanical alteration in reservoir rocks assessed via batch reaction experiments and scratch testing. Greenhouse Gases: Sci. Technol. 8, 133–149.

Arson, C., Vanorio, T., 2015. Chemomechanical evolution of pore space in carbonate microstructures upon dissolution: linking pore geometry to bulk elasticity. J. Geophys. Res. Solid Earth 120, 6878–6894.

Bachu, S., Gunter, W., Perkins, E., 1994. Aquifer disposal of CO2: hydrodynamic and mineral trapping. Energy Convers. Manag. 35, 269–279.

Bostanabad, R., Zhang, Y., Li, X., Kearney, T., Brinson, L.C., Apley, D.W., Liu, W.K., Chen, W., 2018. Computational microstructure characterization and reconstruction: review of the state-of-the-art techniques. Prog. Mater. Sci. 95, 1–41.

Buades, A., Coll, B., Morel, J.-M., 2005. A non-local algorithm for image denoising. In: 2005 IEEE Computer Society Conference on Computer Vision and Pattern Recognition (CVPR'05). IEEE, pp. 60–65.

Burnside, N.M., Shipton, Z.K., Dockrill, B., Ellam, R.M., 2013. Man-made versus natural CO2 leakage: a 400 ky history of an analogue for engineered geological storage of CO2. Geology 41, 471–474.

Busch, A., Kampman, N., Hangx, S., Snippe, J., Bickle, M., Bertier, P., Chapman, H., Spiers, C., Pijnenburg, R., Samuelson, J., 2014. The Green River natural analogue as a field laboratory to study the long-term fate of CO2 in the subsurface. Energy Proc. 63, 2821–2830.

Castellanza, R., Nova, R., 2004. Oedometric tests on artificially weathered carbonatic soft rocks. J. Geotech. Geoenviron. Eng. 130, 728–739.

Chancey, R.T., Stutzman, P., Juenger, M.C., Fowler, D.W., 2010. Comprehensive phase characterization of crystalline and amorphous phases of a Class F fly ash. Cement Concr. Res. 40, 146–156.

Ciantia, M., Hueckel, T., 2013. Weathering of submerged stressed calcarenites: chemo-mechanical coupling mechanisms. Geotechnique 63, 768–785.

Ciantia, M.O., Castellanza, R., Crosta, G.B., Hueckel, T., 2015. Effects of mineral suspension and dissolution on strength and compressibility of soft carbonate rocks. Eng. Geol. 184, 1–18.

Clark, A.C., Vanorio, T., 2016. The rock physics and geochemistry of carbonates exposed to reactive brines. J. Geophys. Res. Solid Earth 121, 1497–1513.

Croizé, D., Bjørlykke, K., Jahren, J., Renard, F., 2010. Experimental mechanical and chemical compaction of carbonate sand. J. Geophys. Res. Solid Earth 115.
Donovan, A.D., Staerker, T.S., Pramudito, A., Li, W., Corbett, M.J., Lowery, C.M., Romero, A.M., Gardner, R.D., 2012. The Eagle Ford Outcrops of West Texas: a Laboratory for Understanding Heterogeneities within Unconventional Mudstone Reservoirs.
Fernandez-Merodo, J., Castellanza, R., Mabssout, M., Pastor, M., Nova, R., Parma, M., 2007. Coupling transport of chemical species and damage of bonded geomaterials. Comput. Geotech. 34, 200–215.
Fuchs, S.J., Espinoza, D.N., Lopano, C.L., Akono, A.-T., Werth, C.J., 2019. Geochemical and geomechanical alteration of siliciclastic reservoir rock by supercritical CO2-saturated brine formed during geological carbon sequestration. Int. J. Greenh. Gas Control 88, 251–260.
Garcia, D.J., Shao, H., Hu, Y., Ray, J.R., Jun, Y.-S., 2012. Supercritical CO 2–brine induced dissolution, swelling, and secondary mineral formation on phlogopite surfaces at 75–95° C and 75 atm. Energy Environ. Sci. 5, 5758–5767.
Gasda, S.E., Bachu, S., Celia, M.A., 2004. Spatial characterization of the location of potentially leaky wells penetrating a deep saline aquifer in a mature sedimentary basin. Environ. Geol. 46, 707–720.
Gastal, E.S., Oliveira, M.M., 2012. Adaptive manifolds for real-time high-dimensional filtering. ACM Trans. Graph. 31, 1–13.
Gaus, I., 2010. Role and impact of CO2–rock interactions during CO2 storage in sedimentary rocks. Int. J. Greenh. Gas Control 4, 73–89.
Grgic, D., 2011. Influence of CO2 on the long-term chemomechanical behavior of an oolitic limestone. J. Geophys. Res. Solid Earth 116.
Gunter, W., Wiwehar, B., Perkins, E., 1997. Aquifer disposal of CO 2-rich greenhouse gases: extension of the time scale of experiment for CO 2-sequestering reactions by geochemical modelling. Mineral. Petrol. 59, 121–140.
Hangx, S., Bakker, E., Bertier, P., Nover, G., Busch, A., 2015. Chemical–mechanical coupling observed for depleted oil reservoirs subjected to long-term CO2-exposure–A case study of the Werkendam natural CO2 analogue field. Earth Planet Sci. Lett. 428, 230–242.
Hangx, S., van der Linden, A., Marcelis, F., Bauer, A., 2013. The effect of CO2 on the mechanical properties of the Captain Sandstone: geological storage of CO2 at the Goldeneye field (UK). Int. J. Greenh. Gas Control 19, 609–619.
Hubbell, J.H., Seltzer, S.M., 1995. Tables of X-Ray Mass Attenuation Coefficients and Mass Energy-Absorption Coefficients 1 keV to 20 MeV for Elements Z= 1 to 92 and 48 Additional Substances of Dosimetric Interest. National Inst. of Standards and Technology-PL, Gaithersburg, MD (United.
Hubler, M.H., Gelb, J., Ulm, F.-J., 2017. Microtexture analysis of gas shale by XRM imaging. J. Nanomech. Micromech. 7, 4017005.
Ilgen, A.G., Aman, M., Espinoza, D.N., Rodriguez, M.A., Griego, J., Dewers, T.A., Feldman, J.D., Stewart, T., Choens, R., Wilson, J., 2018. Shale-brine-CO2 interactions and the long-term stability of carbonate-rich shale caprock. Int. J. Greenh. Gas Control 78, 244–253.
Ilgen, A.G., Cygan, R.T., 2016. Mineral dissolution and precipitation during CO2 injection at the Frio-I Brine Pilot: geochemical modeling and uncertainty analysis. Int. J. Greenh. Gas Control 44, 166–174.
Kampman, N., Busch, A., Bertier, P., Snippe, J., Hangx, S., Pipich, V., Di, Z., Rother, G., Harrington, J., Evans, J.P., 2016. Observational evidence confirms modelling of the long-term integrity of CO 2-reservoir caprocks. Nat. Commun. 7, 12268.
Kharaka, Y.K., Cole, D.R., Hovorka, S.D., Gunter, W., Knauss, K.G., Freifeld, B., 2006. Gas-water-rock interactions in Frio Formation following CO2 injection: implications for the storage of greenhouse gases in sedimentary basins. Geology 34, 577–580.
Lamy-Chappuis, B., Angus, D., Fisher, Q.J., Yardley, B.W., 2016. The effect of CO2-enriched brine injection on the mechanical properties of calcite-bearing sandstone. Int. J. Greenh. Gas Control 52, 84–95.
Le Gallo, Y., Couillens, P., Manai, T., 2002. CO2 sequestration in depleted oil or gas reservoirs. In: SPE International Conference on Health, Safety and Environment in Oil and Gas Exploration and Production. Society of Petroleum Engineers.
Lee, S.S., Schmidt, M., Sturchio, N.C., Nagy, K.L., Fenter, P., 2019. Effect of pH on the formation of gibbsite-layer films at the muscovite (001)–water interface. J. Phys. Chem. C 123, 6560–6571.
Li, Q., Lim, Y.M., Flores, K.M., Kranjc, K., Jun, Y.-S., 2015. Chemical reactions of portland cement with aqueous CO2 and their impacts on cement's mechanical properties under geologic CO2 sequestration conditions. Environ. Sci. Technol. 49, 6335–6343.
Li, X., Peng, C., Crawshaw, J.P., Maitland, G.C., Trusler, J.M., 2018. The pH of CO2-saturated aqueous NaCl and NaHCO3 solutions at temperatures between 308 K and 373 K at pressures up to 15 MPa. Fluid Phase Equil. 458, 253–263.
Liu, F., Lu, P., Griffith, C., Hedges, S.W., Soong, Y., Hellevang, H., Zhu, C., 2012. CO2–brine–caprock interaction: reactivity experiments on Eau Claire shale and a review of relevant literature. Int. J. Greenh. Gas Control 7, 153–167.
Lu, J., Kharaka, Y.K., Thordsen, J.J., Horita, J., Karamalidis, A., Griffith, C., Hakala, J.A., Ambats, G., Cole, D.R., Phelps, T.J., 2012. CO2–rock–brine interactions in Lower Tuscaloosa Formation at Cranfield CO2 sequestration site, Mississippi, USA. Chem. Geol. 291, 269–277.
Lydon, J., 2005. The measurement of the modal mineralogy of rocks from SEM imagery: the use of Multispec© and ImageJ freeware. Geol. Surv. Can. Open File 4941, 37.
Martogi, D., Abedi, S., 2019. Indentation based method to determine the mechanical properties of randomly oriented rock cuttings. In: 53rd US Rock Mechanics/Geomechanics Symposium. American Rock Mechanics Association.
Martogi, D., Abedi, S., 2020. Microscale approximation of the elastic mechanical properties of randomly oriented rock cuttings. Acta Geotechnica 15, 3511–3524.
Mashhadian, M., Abedi, S., Noshadravan, A., 2018a. Probabilistic multiscale characterization and modeling of organic-rich shale poroelastic properties. Acta Geotechnica 13, 781–800.
Mashhadian, M., Verde, A., Sharma, P., Abedi, S., 2018b. Assessing mechanical properties of organic matter in shales: results from coupled nanoindentation/SEM-EDX and micromechanical modeling. J. Petrol. Sci. Eng. 165, 313–324.
Memon, K.R., Ali, M., Awan, F.U.R., Mahesar, A.A., Abbasi, G.R., Mohanty, U.S., Akhondzadeh, H., Tunio, A.H., Iglauer, S., Keshavarz, A., 2021. Influence of cryogenic liquid nitrogen cooling and thermal shocks on petro-physical and morphological characteristics of Eagle Ford shale. J. Nat. Gas Sci. Eng. 96, 104313.
Minardi, A., Stavropoulou, E., Kim, T., Ferrari, A., Laloui, L., 2021. Experimental assessment of the hydro-mechanical behaviour of a shale caprock during CO2 injection. Int. J. Greenh. Gas Control 106, 103225.
Nordbotten, J.M., Celia, M.A., Bachu, S., Dahle, H.K., 2005. Semianalytical solution for CO2 leakage through an abandoned well. Environ. Sci. Technol. 39, 602–611.
Prakash, R., Nguene, P.C.K., Benoit, D., Henkel, K., Abedi, S., 2021. Assessment of local phase to mechanical response link: application to the chemo-mechanical identification of rock phases subjected to reactive environments. J. Nat. Gas Sci. Eng. 103857.
Rosenbauer, R.J., Koksalan, T., Palandri, J.L., 2005. Experimental investigation of CO2–brine–rock interactions at elevated temperature and pressure: implications for CO2 sequestration in deep-saline aquifers. Fuel Process. Technol. 86, 1581–1597.
Saxena, N., Hofmann, R., Alpak, F.O., Dietderich, J., Hunter, S., Day-Stirrat, R.J., 2017. Effect of image segmentation & voxel size on micro-CT computed effective transport & elastic properties. Mar. Petrol. Geol. 86, 972–990.
Schindelin, J., Arganda-Carreras, I., Frise, E., Kaynig, V., Longair, M., Pietzsch, T., Preibisch, S., Rueden, C., Saalfeld, S., Schmid, B., 2012. Fiji: an open-source platform for biological-image analysis. Nat. Methods 9, 676.
Scientific, T.F., 2015. Avizo Software 9.0 Release Notes. Thermo Fisher Scientific, Hillsboro, OR.
Scientific, T.F., 2018. Amira-Avizo Software. Thermo Scientific™ Amira-Avizo Software.
Sharma, P., Prakash, R., Abedi, S., 2019. Effect of temperature on nano-and microscale creep properties of organic-rich shales. J. Petrol. Sci. Eng. 175, 375–388.
Shvartsev, S., 2012. Internal evolution of the water-rock system: nature and mechanisms. Earth Sci. Res. 1, 106.
Slim, M., Abedi, S., Bryndzia, L.T., Ulm, F.-J., 2018. Role of organic matter on nanoscale and microscale creep properties of source rocks. J. Eng. Mech. 145, 4018121.
Vanorio, T., 2015. Recent advances in time-lapse, laboratory rock physics for the characterization and monitoring of fluid-rock interactions. Geophysics 80, WA49–WA59.
Vialle, S., Vanorio, T., 2011. Laboratory measurements of elastic properties of carbonate rocks during injection of reactive CO2-saturated water. Geophys. Res. Lett. 38.
Wang, W., Li, J., Fan, M., Abedi, S., 2017. Characterization of electrical properties of organic-rich shales at nano/micro scales. Mar. Petrol. Geol. 86, 563–572.
Westenberger, P., 2008. AVIZO-3D visualization framework. In: Geoinformatics Conference, pp. 1–11.